ACS APPLIED MATERIALS & INTERFACES

www.acsami.org

Research Article

NiMo−NiCu Inexpensive Composite with High Activity for Hydrogen Evolution Reaction

Hugo L. S. Santos, Patricia G. Corradini, Marina Medina, Jeferson A. Dias, and Lucia H. Mascaro*

Cite This: *ACS Appl. Mater. Interfaces* 2020, 12, 17492−17501

Read Online

ACCESS | Metrics & More | Article Recommendations | Supporting Information

ABSTRACT: In this work, the effect of copper addition on NiMo coating is evaluated in regard to the hydrogen evolution reaction (HER). NiMo and NiMo−NiCu composites are prepared by a simple coelectrodeposition process. The effect of Cu on deposit characters were tested by varying it in the range of 0.06−0.20 molar ratio. Copper addition promotes the growth of a new crystalline phase: NiCu. Also, the copper addition changed the composite surface. NiMo−$NiCu_{0.12}$ shows a surface roughness 30 times higher than the NiMo material. NiMo−NiCu materials present higher activity toward HER, larger electroactive area, and higher stability in continuous water electrolysis than NiMo catalysts, as demonstrated by Tafel curves, electrochemical impedance spectroscopy measurements, and polarization tests. The combination of the large electroactive area due to the copper addition, the synergism between Ni−Mo, and the presence of Ni and Mo oxides on the surface results in catalyst with excellent features for HER application.

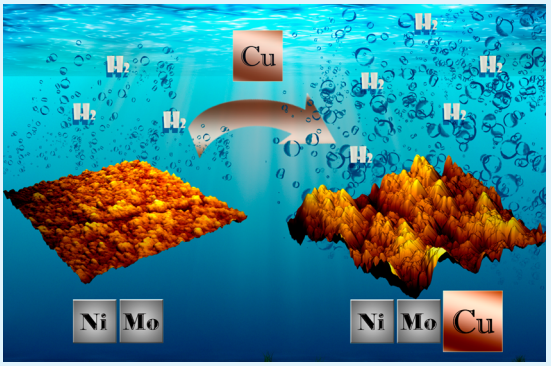

KEYWORDS: *electrodeposition, coating film, nickel alloys, molybdenum alloys, copper alloys, hydrogen evolution reaction, water splitting, alkaline media*

1. INTRODUCTION

The environmental and socioeconomic issues concerning the intensive use of fossil fuels show that it is necessary to find alternatives for the current world energy matrix. Hydrogen (H_2), which has no carbon emission, is recognized as the most promising alternative fuel in the renewable energy-based economy.[1,2] Water electrolysis is an interesting and useful method to obtain pure H_2, for sustainable development. However, strategies to obtain an economical and efficient hydrogen evolution reaction (HER) rate are important for practical application and perform as the link between low overpotential and high efficiency.[3,4]

Electrocatalysts can be used to improve the rates for HER and make the process more attractive for practical application. A desired material for this application should present good electrical conductivity, high corrosion resistance, large active surface area, low overpotential, and low price.[5−7] Noble metals, such as platinum, present high catalytic activity for hydrogen production. However, high prices and scarcity limit their use for large-scale production.[8]

Nickel is the most used cathode material for water electrolysis in alkaline medium, mainly due to its low price and good corrosion resistance.[9−12] It has been observed that the catalytic activity of the transition metals increases with the number of d electrons and reaches maximum potential near full electronic filling.[13,14] However, the hydrogen evolution rate also depends on the hydrogen adsorption step, which increases as the d orbital electronic filling decreases. It is possible to improve the electroactivity of metals with high d orbital electronic filling to increase the number of vacancies, which can be responsible for strong interaction with electron-donating atoms and adsorb hydrogen by electron pairs formation.[13,15] Another way is to combine transition metals that present semifilled d orbitals (Mo, W, and others) with transition metals having pairs of paired electrons (Fe, Co, Ni, and Cu), which show high synergism and excellent catalytic activity for HER applications.[2,13,16−21] The addition of copper has become an alternative to improve the efficiency of Ni-based catalysts, due to the surface area modification and/or electrocatalytic synergism effect of metal alloying.[21−23] For example, Xia et al. investigated the catalytic activity of the Ni−Mo−Cu alloy for the hydrogen evolution reaction. The Ni−Mo−Cu alloy showed a 10-fold increase in the film roughness concerning the Ni−Mo alloy. Analyzing the catalytic activity for the HER of both films, the Ni−Mo−Cu alloy showed an improvement in the catalysis verified by the increase in the current density.[20] However, it is not clear how this element is

Received: January 9, 2020
Accepted: March 27, 2020
Published: March 27, 2020

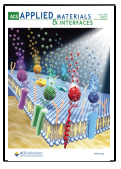

https://dx.doi.org/10.1021/acsami.0c00262
ACS Appl. Mater. Interfaces 2020, 12, 17492−17501

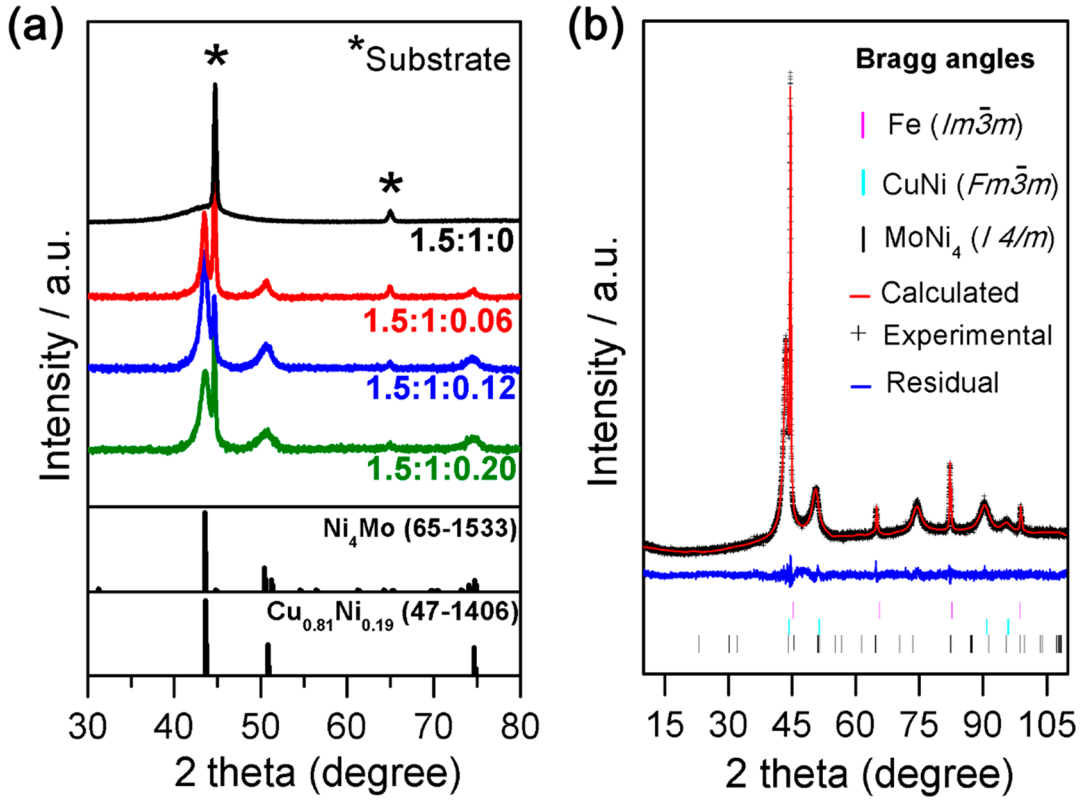

Figure 1. Structural characterization: (a) XRD profiles of Ni−Mo and Ni−Mo−Cu electrodes, with different Ni:Mo:Cu bath ratios. (b) Rietveld refinement of NiMo−$NiCu_{0.12}$ XRD profile.

distributed in the material: if there is a formation of ternary metal alloy, or the presence of oxides already acts as a catalyst; and more studies are needed about the real role of copper in the NiMo catalysts activity increasing toward HER.

The electrodeposition is an interesting and efficient method for coatings preparation because it has a one-step fabrication process at room pressure and temperature, and it can be easily incorporated into a full water splitting device.[24,25] Moreover, it is possible to control and analyze the thickness, phase structure, and morphology of the cathode material.[26] In this work, the coelectrodeposition of NiMo−NiCu catalysts is reported and the aim is to analyze the copper influence on the morphology and in the HER catalytic performance of the resulting materials. The catalysts are physically characterized using scanning electron microscopy (SEM) and atomic force microscopy (AFM), X-ray fluorescence (XRF), X-ray diffraction (XRD), X-ray photoelectron spectroscopy (XPS), polarization curves, and electrochemical impedance spectroscopy (EIS).

2. MATERIALS AND METHODS

2.1. Preparation of the NiMo and NiMo−NiCu Electrodes. NiMo−NiCu films were obtained by electrodeposition on a single compartment electrochemical cell, with $Ag_{(s)}|AgCl_{(s)}|KCl_{(sat.)}$ and Pt grid as reference and counter electrode, respectively. Resin embedded carbon steel 1010 (0.196 cm^2) was used as the working electrode. Before electrodeposition, the steel electrodes were treated with 5% v/v H_2SO_4 solution, polished with 600 grit sandpaper, and immersed for 5 min in 30% w/v KOH, for alkaline degreasing.

The deposition baths were prepared with similar Ni:Mo molar ratio for all films (1.5:1), and at different molar ratios of Cu (0; 0.06; 0.12; 0.20). The films were named according to the copper molar ratio, NiMo for copper-free film and NiMo−$NiCu_{0.06}$, NiMo−$NiCu_{0.12}$, and NiMo−$NiCu_{0.2}$ for copper-containing films. The precursors of metal deposition were as follows: 0.15 mol L^{-1} nickel(II) sulfate hexahydrate ($NiSO_4{\cdot}6H_2O$; 98%), 0.1 mol L^{-1} sodium molybdate (Na_2MoO_4, 99%), and 0.006, 0.012, and 0.02 mol L^{-1} copper(II) sulfate pentahydrate ($CuSO_4{\cdot}5H_2O$, 99%). 0.3 mol L^{-1} sodium citrate ($Na_3C_6H_5O_7$) was used as complexing agent and 0.3 mol L^{-1} NaCl as support electrolyte, as recommended in the literature.[20,27] The pH of the bath was adjusted to 8.75 with NH_4OH for all studied compositions. All coatings, NiMo and NiMo−NiCu composites, were obtained galvanostatically at −50 mA cm^{-2} in 40 min, at room temperature.

2.2. Physical Characterization of NiMo and NiMo−NiCu Catalysts. The morphology characterization of the electrodes was performed by SEM with high resolution field emission using a FEG-SEM ZEISS SUPRA 35. The topography and roughness of the films were analyzed by AFM using a Bruker (Nanoscope V) microscope in contact mode. The roughness of the coatings was obtained using Gwyddion software, v 2.53.[28]

The two-dimensional mapping of the chemical composition of NiMo−NiCu was estimated by X-ray dispersive energy spectroscopy (EDS), on FEI-XL30-FEG coupled to the detector Oxford Instruments-Link ISIS 300. Additionally, qualitative and quantitative (Cu, Ni, Mo) elemental analysis were performed by X-ray fluorescence (XRF) in a Shimadzu EDX-720 instrument. The whole surface of the films was utilized for quantification. The crystallographic characterizations were obtained by XRD, using the Rigaku - DMax2500PC (Cu Kα, 1.5406 Å, 40 kV). XPS measurements were carried out on spectrometer Scienta Omicron, model ESCA 2SR. The Mg Kα monochromator, calibrated using the C 1 peak (284.8 eV), was used to provide the incident photon energy.

2.3. Electrochemical Characterizations of NiMo and NiMo−NiCu Catalysts. The HER activity for NiMo and NiMo−NiCu composites was evaluated in a three-electrode electrochemical cell, like that used for deposition. For this measurement, a Hg/HgO/KOH 6 M electrode was used as the reference electrode. Stationary point-to-point cathodic polarization curves were performed in 6.0 mol L^{-1}

https://dx.doi.org/10.1021/acsami.0c00262
ACS Appl. Mater. Interfaces 2020, 12, 17492−17501

KOH at 25 °C. For each point, a chronopotentiometry measurement of 6 min was performed, and 20 points were collected in the range of current densities between -1×10^{-6} and -1.0 A cm^{-2}. Prior to the polarization curves, the electrodes were polarized at −1.3 V vs Hg/HgO for 10 min. Electrochemical impedance spectroscopy (EIS) measurements were also performed to elucidate the charge-transfer resistance and HER mechanism aspects. The EIS parameters were obtained in 6.0 mol L^{-1} KOH; 25 °C; at −0.928, −1.028, and −1.078 V (vs Hg/HgO); amplitude of 10 mV; and frequency range of 10 kHz to 0.1 Hz.

In order to evaluate the influence of temperature on the catalytic activity of these deposits, cathodic polarization curves between −0.9 and −1.2 V (vs Hg/HgO) were performed with 0.5 mV s^{-1} at 293, 303, 313, 323, and 333 K. The activation energy for the HER of these deposits was determined by the Arrhenius equation.[29] The double-layer capacitance (C_{dl}) used to estimate the electrochemical active surface area (ECSA) was determined by cyclic voltammetry (CV) in the capacitive range of −0.6 to −0.7 V (vs Hg/HgO) at the scan rates of 10, 50, 100, and 150 mV s^{-1}. To obtain the C_{dl}, the capacitive density current average (Δj), adopted that $\Delta j = |j_c - j_a|/2$, where j_c is the cathodic density current and j_a is the anodic density current, at −0.65 V (vs Hg/HgO). Δj was plotted versus different scan rates and the obtained linear slope value was equivalent to C_{dl}.[30,31] The ECSA was estimated using the relation ECSA = C_{dl}/C_S, where the C_S value is known as C_S = 0.040 mF cm^{-2} per cm^2_{ECSA}.[31,32] The stability of NiMo and NiMo−$NiCu_{0.12}$ was evaluated by continuous electrolysis conducted in 6.0 mol L^{-1} KOH for 48 h, applying a constant current density of −100 mA cm^{-2}.

3. RESULTS AND DISCUSSION

3.1. Crystalline Structure, Morphology, and Composition of NiMo and NiMo−NiCu Catalysts. The crystalline structures of the NiMo and Ni−Mo−Cu films are characterized by XRD analysis. Figure 1a shows the XRD patterns for NiMo and Ni−Mo−Cu deposited from different amounts of Cu(II) in the solution. For the NiMo film (black line), only a broad peak at 43.5° is recorded, that is attributed to the diffraction of the $MoNi_4$ (JCPDS No. 65-1533). The broadening of the this peak indicates an amorphous/nanocrystalline nature for this phase.[33] On the other hand, all Ni−Mo−Cu coatings (red, blue, and green lines) presented peaks that can be attributed to $MoNi_4$ and NiCu (JCPDS 65-7246) phases.[20] The CuNi and $MoNi_4$ phases show very similar crystallographic patterns (Figure 1a); hence, it is difficult to take indicatives of which phase is predominant in Ni−Mo−Cu films. Therefore, Rietveld refinement is performed for all obtained films in order to better characterize the crystalline phases, as presented in Figure S1, available in the Supporting Information (SI). As an example, Figure 1b presents the Rietveld profile for Ni−Mo−Cu film obtained at 0.12 mol L^{-1} Cu solution bath, showing the experimental and calculated data. The residual curve (blue line) is very smooth and the experimental and calculated curves are overlapped; these results indicate that the calculated XRD pattern fits very well with the experimental data. Moreover, the statistical parameter weighted profile *R*-factor (R_{wp}) is very low at 4.19%, as the goodness-of-fit (χ^2) is 1.43. Low values for R_{wp} as obtained in this work and χ^2 close to unity indicate an excellent refinement, and similar results were obtained for other samples shown in Figure S1 (in SI). Quantitative analysis of crystalline phases has revealed that Ni−Mo−$Cu_{0.12}$ film is composed of a mixture of 98.23% Cu−Ni phase with predicted stoichiometry of $Cu_{0.53}Ni_{0.47}$ and 1.77% $MoNi_4$ phase, discounting the substrate signal. This result indicates that like the NiMo film, the NiMo phases formed in the Ni−Mo−Cu composite are mostly amorphous or nanocrystalline. The high content of Ni and Mo quantified by XRF is therefore mostly related to amorphous Ni−Mo phase that cannot be properly quantified by X-ray diffraction. The absence of Cu−Mo phases can be explained by the thermodynamics. The Cu−Mo phase is an immiscible system (has a positive entropy of mixing); therefore, its production requires highly energetic methods and it cannot be obtained by electrodeposition.[34] Taking into account the fact that the Mo(VI) ions in the deposition baths are not reduced to metallic Mo separately, it is reasonable to conclude that the deposition of the NiMo−NiCu film probably occurred in two processes: Ni−Cu regular deposition and Ni−Mo amorphous/nanocrystalline phases induced deposition. Thus, to avoid any allusion to the ternary alloy formation, the samples Ni−Mo−Cu will be named as NiMo−$NiCu_{0.06}$, NiMo−$NiCu_{0.12}$, and NiMo−$NiCu_{0.2}$, which subscribed value indicates the copper concentration of the deposition bath.

The effect of copper on the morphology of NiMo coatings is verified by scanning electron microscopy (SEM). SEM images for all coatings can be seen in Figure 2a−d. The NiMo coating

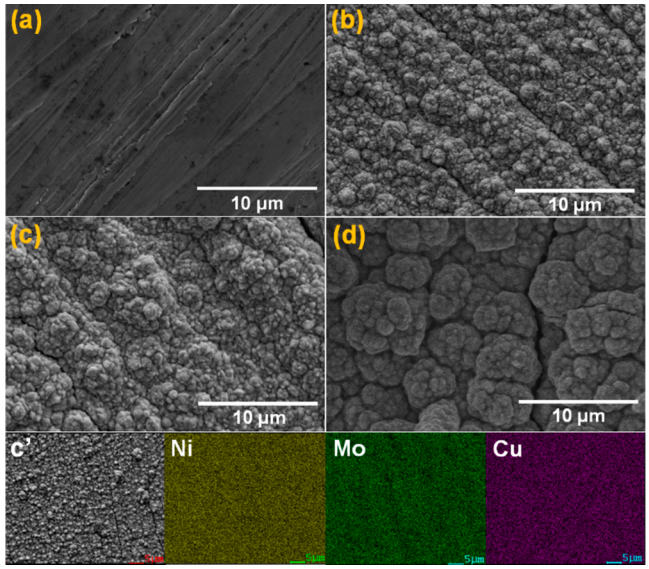

Figure 2. Scanning electron micrographs of (a) NiMo, (b) NiMo−$NiCu_{0.06}$, (c) NiMo−$NiCu_{0.12}$, and (d) NiMo−$NiCu_{0.20}$. (c′) Two-dimensional mapping chemical composition of NiMo−$NiCu_{0.12}$ coating.

surface (Figure 2a) is smooth, with grains so small they cannot be seen with the applied magnification, a typical characteristic of this material.[35,36] In contrast, the coatings obtained in the baths containing copper present compact, irregular, and cracked surfaces; with well-defined grain outlines. For these cases, grains with rounded or cauliflower shapes depending on the copper concentration are presented, as seen in Figure 2b−d. Grains become larger as the concentration of copper in the bath increases; for example, the NiMo−$NiCu_{0.12}$ film has rounded grains of different sizes (Figure 2b). On the other hand, the NiMo−$NiCu_{0.2}$ coating shows larger cauliflower-shaped structures (Figure 2d). Due to irregular structures of the NiMo−NiCu coatings, it is expected that there will be a difference in the surface area of these catalysts compared to NiMo, which may promote changes in the catalytic activities for HER. It is possible to assert that the distribution of nickel, copper, and molybdenum is homogeneous on the whole

https://dx.doi.org/10.1021/acsami.0c00262
ACS Appl. Mater. Interfaces 2020, 12, 17492−17501

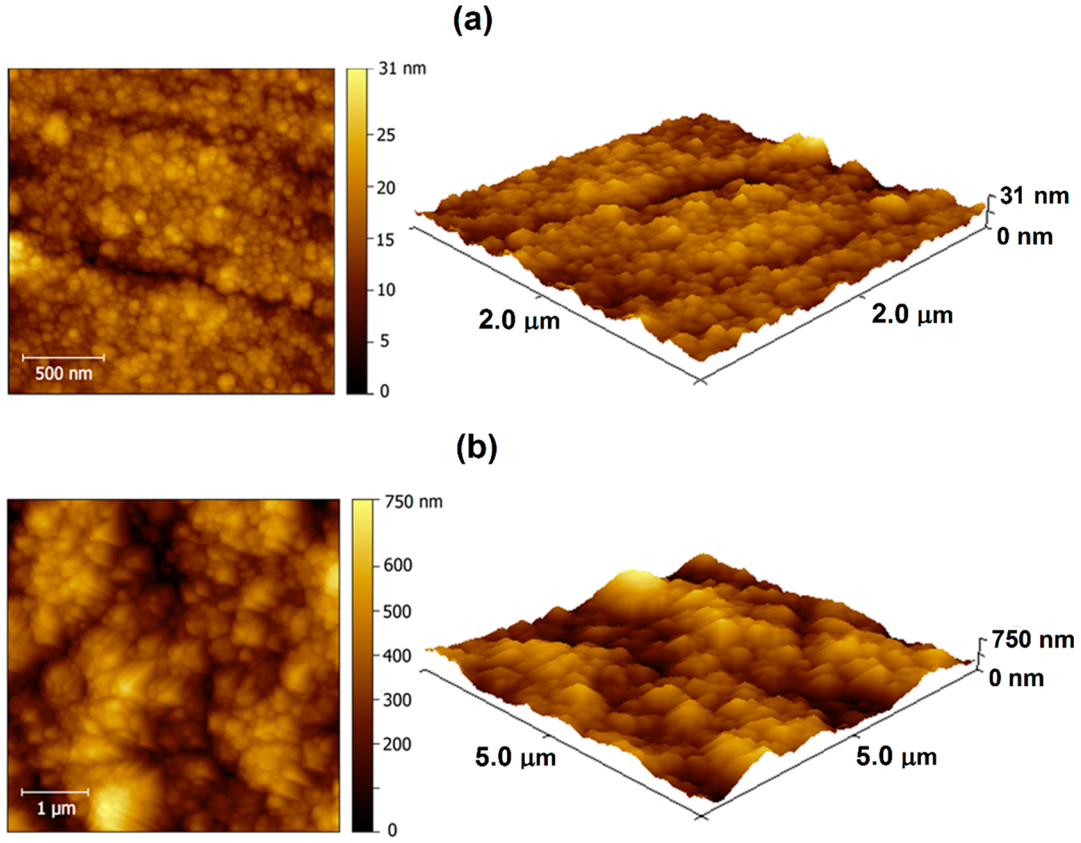

Figure 3. 2D and 3D AFM images for (a) NiMo and (b) NiMo−$NiCu_{0.12}$.

substrate surface from EDS two-dimensional mapping of NiMo−$NiCu_{0.12}$ (Figure 2c′).

In order to further investigate the influence of copper on the topography and roughness of NiMo coatings, AFM is performed for NiMo and NiMo−$NiCu_{0.12}$ films. The 2D and 3D micrographs are shown in Figure 3. According to the XRD data, the NiMo grains, observed at Figure 3a, present a nanocrystalline structure. NiMo coating presents a smoother surface with smaller grains compared to the NiMo−$NiCu_{0.12}$ coating (Figure 3b). The addition of copper to the NiMo coating promotes a modification in the topography of the NiMo film, since the small rounded NiMo grains become large pyramidal grains in the NiMo−$NiCu_{0.12}$ coatings. The average roughness is estimated as 2.68 nm for NiMo and 99.01 nm for NiMo−NiCu. Hence, the addition of copper results in a significant morphological change and surface roughness increases by 30 times. Even though the catalytic activity of copper for HER[20,23,32] is low, its addition leads to an increment in the NiMo−NiCu electroactive area, which plays an important role for electrocatalysis.

The compositions of the coatings are estimated by XRF. Qualitative analysis showed the presence of Ni, Cu, and Mo, typical from the films; and Fe, S, Ca, P, and Mn from the substrate. The quantitative results are presented in Table 1. The instrumental imprecisions are also shown along with the respective atomic percentage. Although the amount of Cu(II) is almost 10 times lower than concentrations of Ni(II) and Mo(VI) in the deposition baths, a large amount of copper is deposited for all films. Copper is thermodynamically more noble than Ni and Mo, which favors its deposition. Increasing Cu(II) concentration in the baths had a negligible effect on the deposition of Ni. About low Cu concentration electrolytes, the

Table 1. Chemical Composition Determined by Quantitative-XRF for NiMo and NiMo−NiCu Films Electrodeposited at −50 mA cm^{-2} on Steel 1010 Substrate

sample	Ni (at%)	Mo (at%)	Cu (at%)
NiMo	77.4 ± 0.7	22.6 ± 0.2	
NiMo−$NiCu_{0.06}$	53.6 ± 0.3	10.10 ± 0.09	36.3 ± 0.2
NiMo−$NiCu_{0.12}$	55.0 ± 0.2	9.30 ± 0.06	35.7 ± 0.2
NiMo−$NiCu_{0.20}$	50.0 ± 0.2	7.3 ± 0.1	42.7 ± 0.2

literature reports that the Cu deposition takes place at the limiting current. However, at a sufficient cathodic range, as applied in this work, the partial current density of Ni(II) reduction becomes higher than the current density of Cu(II) reduction, thus increasing the Ni content of the film.[37] However, the amount of molybdenum on the films decreases when Cu(II) concentration in the baths increases; the deposits present small contents of this element, from 7.3% to 10.1%. The difference in the chemical composition quantified by XRF and by X-ray diffraction is mostly related to the amorphous Ni−Mo phase that cannot be properly applied for XRD technique. It should be noted that the composition estimated by XFR is not necessarily the same as the surface composition, where the catalytic reactions occur.

XPS spectra of Ni 2p, Mo 3d, and Cu 2p of NiMo−$NiCu_{0.12}$ film is presented in Figure 4. The Ni 2p spectrum deconvolution is presented in Figure 4a. It is meaningful that some shifts can be observed in this spectrum; it is a result of binding energy of Ni 2p species that can occur due to the slight electron transfer from Mo and Cu to Ni,[38] probably related to the NiMo and NiCu alloys presence in the bulk. Two species are detected on Ni $2p_{3/2}$ region: NiO (855.4 eV) and NiOOH

https://dx.doi.org/10.1021/acsami.0c00262
ACS Appl. Mater. Interfaces 2020, 12, 17492−17501

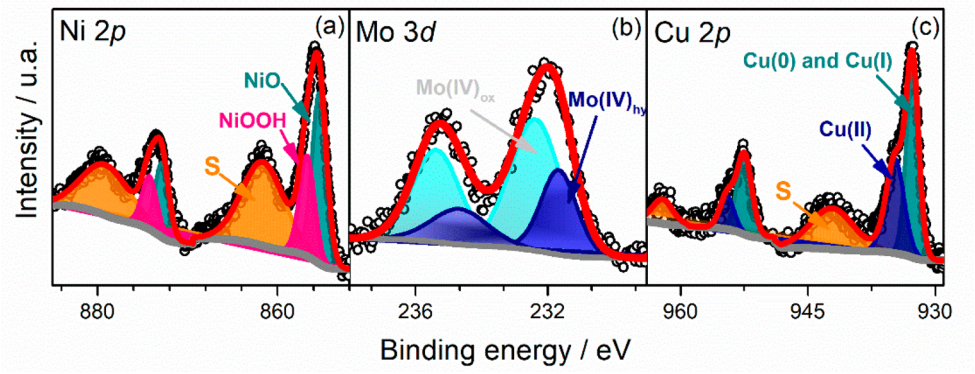

Figure 4. X-ray photoelectron region spectra of NiMo−$NiCu_{0.12}$ film: (a) Nickel 2p, (b) molybdenum 3d, and (c) copper 2p.

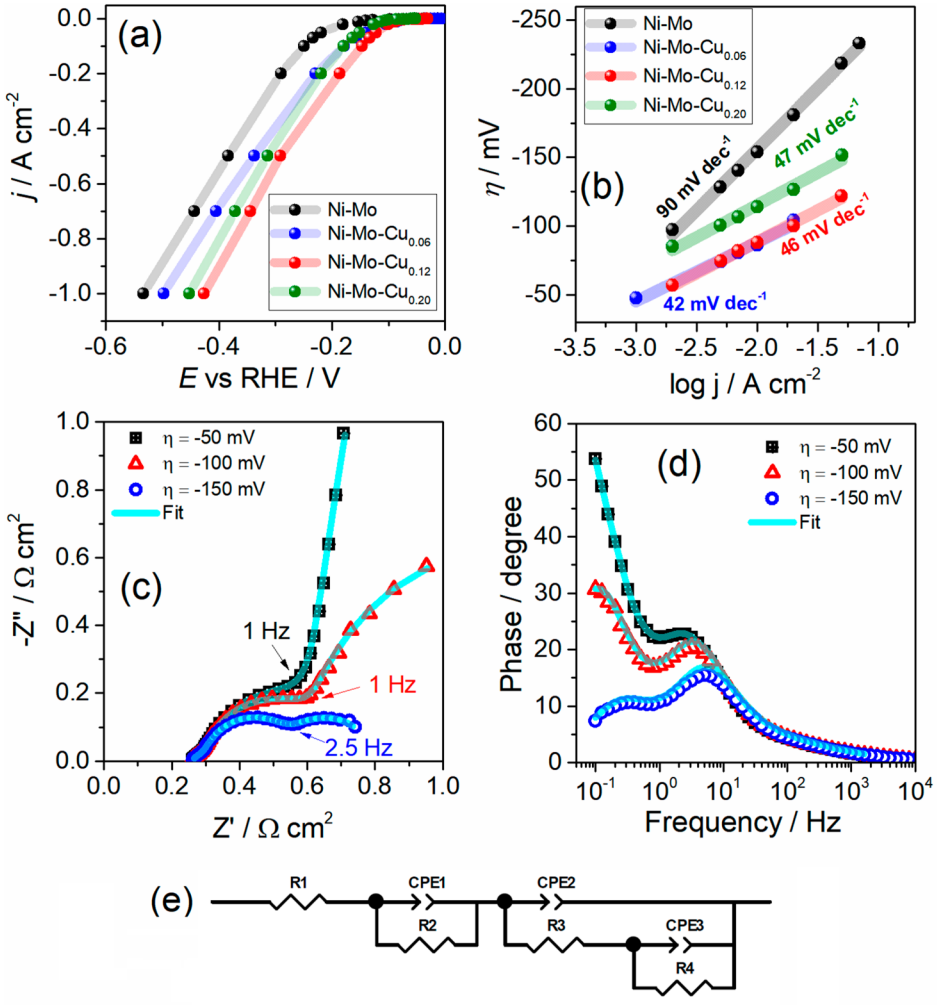

Figure 5. (a) Point-to-point cathodic linear curves and (b) Tafel curves for the NiMo and NiMo−NiCu films, in KOH 6.0 mol L^{-1}, 25 °C. (c) Nyquist and (d) Bode diagrams for the NiMo−$NiCu_{0.12}$ in 6.0 mol L^{-1} KOH. (e) Equivalent circuit proposed for EIS measurements.

(856.7 eV).[38,39] Peaks at 861.8 and 879.3 eV refer to shakeup satellites.[40,41] Nickel in metal form was not detected for XPS, indicating that the surface of the material presents both oxidized and hydroxide forms (NiO or NiOOH), as some papers suggest.[42,43] Mo 3d spectra (Figure 4b) are deconvoluted in two duplets: at 231.6 and 232.4 eV on Mo $3d_{5/2}$ region. Both signals are related to Mo(IV) species in hydroxide and oxidized forms, respectively.[44] Referring to the Cu $2p_{3/2}$ region, reduced copper species (Cu(0) and Cu(I)) are observed at 932.8 eV, while the peak located at 934.7 eV is related to Cu(II) (Figure 4c).[45−47] The existence of satellite peak located at about 942 eV confirms the presence of Cu(II).[48] The sensitivity of the XPS technique does not allow for an analysis of the composition in depth profile,[44] but confirms the presence of all species on the surface of the catalyst. The surface atomic composition of catalysts estimated for XPS measurements is Ni:Mo:Cu 71:10:19.

https://dx.doi.org/10.1021/acsami.0c00262
ACS Appl. Mater. Interfaces 2020, 12, 17492−17501

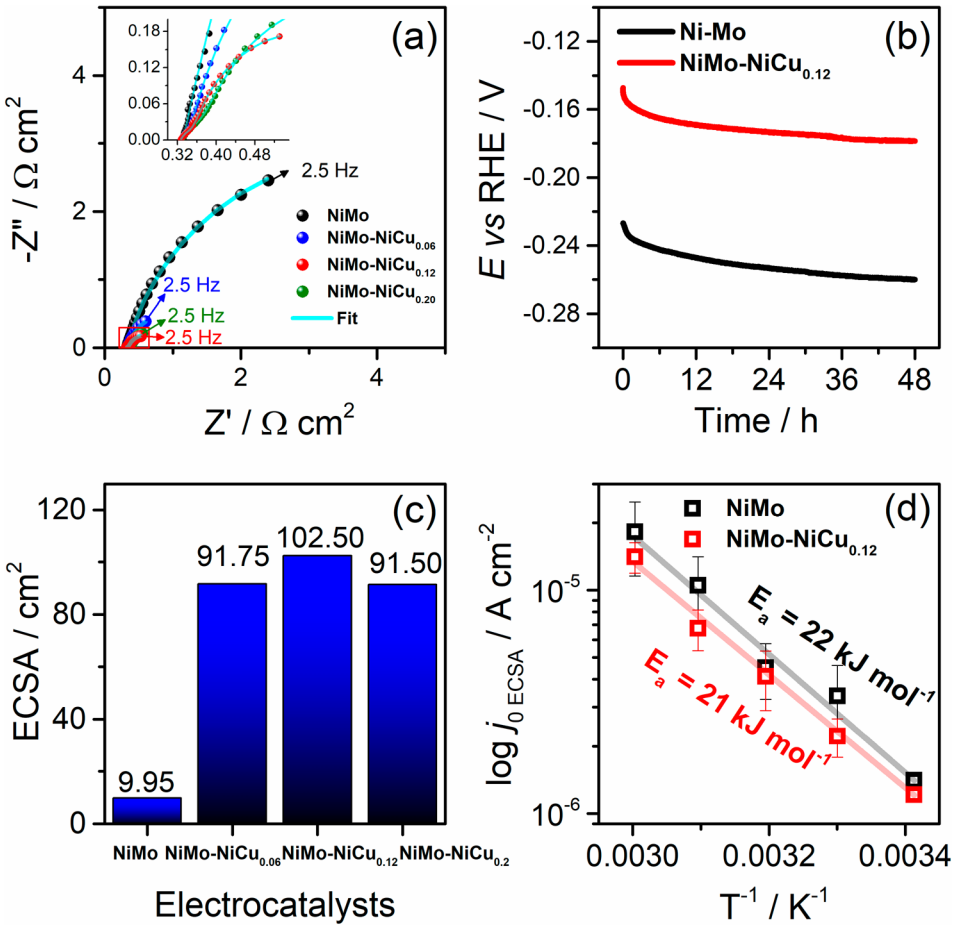

Figure 6. (a) Nyquist plot for all NiMo−NiCu films, at −0.1 V vs RHE in 6.0 mol L^{-1} KOH. (b) Continuous water electrolysis at −100 mA cm^{-2} for NiMo and NiMo−$NiCu_{0.12}$ catalysts. (c) Electrochemical active surface areas (ECSA) for all obtained materials. (d) Arrhenius graph for NiMo−$NiCu_{0.12}$ and NiMo coatings.

3.2. HER Activity of NiMo and NiMo−NiCu Catalysts. Stationary cathodic polarization measurements are performed on 6.0 mol L^{-1} KOH electrolyte to investigate the HER activity of NiMo and NiMo−NiCu coatings. These curves are made point-to-point in the range of current densities -1×10^{-6} to −1.0 A cm^{-2} without IR-drop correction. The potentials are converted to reversible hydrogen electrode (RHE) using the following equation:

$$E_{RHE} = E_{Hg/HgO} + 0.928 \quad (1)$$

where $E_{Hg/HgO}$ is the potential versus Hg/HgO reference electrode. The value of 0.928 was found by calibrating the reference electrode in a hydrogen-saturated 6.0 mol L^{-1} KOH solution, as presented in Figure S2 in Supporting Information. Figure 5a shows the polarization curves with the required overpotential for all coatings. The NiMo composite shows the lowest HER activity presenting an overpotential of −154 and −250 mV at the current values of −10 and −100 mA cm^{-2}, respectively. It can also be observed that NiMo−$NiCu_{0.06}$ presents the lowest overpotential (−86 mV) at −10 mA cm^{-2} when compared to NiMo (−154 mV), NiMo−$NiCu_{0.12}$ (−88 mV), and NiMo−$NiCu_{0.2}$ (−114 mV). However, for higher overpotentials, an inversion in the HER activity of NiMo−NiCu films is noted. The NiMo−$NiCu_{0.12}$ film shows a small overpotential (−147 mV) to deliver the current density of −100 mA cm^{-2} as compared to NiMo (−250 mV), NiMo−$NiCu_{0.06}$ (−179 mV), and NiMo−$NiCu_{0.2}$ (−178 mV). It is noteworthy that a very low overpotential (−439 mV) is required to achieve a current density of −1.0 A cm^{-2} by utilizing the NiMo−$NiCu_{0.12}$ film as electrocatalyst. Although the NiMo−$NiCu_{0.06}$ film presents better HER activity at low current density, its apparently smoother morphology (as seen in the SEM images, Figure 2) compared to NiMo−$NiCu_{0.12}$ and NiMo−$NiCu_{0.2}$ requires higher overpotential to achieve high current density. It is important to note that the presence of molybdenum is very important for the hydrogen evolution process. As an example, Figure S3 (in SI) compares the cathodic polarization of NiMo−$NiCu_{0.12}$ and $NiCu_{0.12}$ catalysts, and it is clear the overpotential increasing toward the HER process. The low overpotential to achieve −100 mA cm^{-2} of the NiMo−$NiCu_{0.12}$ ranks this material among the most active compounds recently reported, based on non-noble metal electrocatalyst for basic media. The value is comparable to materials such as $Ni_{48}Mo_{15.6}Cu_{36.4}$ (−200 mV),[20] Ni(Cu)/NF (−115 mV),[32] (Ni−Fe)S_x/NiFe(OH)$_y$ (−124 mV),[49] B,N:Mo_2C@BCN (−198 mV),[50] $NiFeO_x$/CFP (−220 mV),[51] N-MoO_2/Ni_3S_2/NF (−300 mV),[52] and NiS/porous Cu (−301 mV).[53] Table S1 shows a comparison with some data reported in the literature for Ni-based catalysts.

To clarify the HER kinetics, Tafel plots were constructed from the polarization curves (Figure 5a) and are shown in Figure 5b. The values of the Tafel slopes are good indicators of reaction rate, besides bringing inferences about the mechanism in which HER is processed. As seen in Figure 5b, the NiMo

https://dx.doi.org/10.1021/acsami.0c00262
ACS Appl. Mater. Interfaces 2020, 12, 17492−17501

film exhibits a high Tafel slope of 90 mV dec^{-1}, which is higher than that of NiMo−$NiCu_{0.06}$ (42 mV dec^{-1}), NiMo−$NiCu_{0.12}$ (46 mV dec^{-1}), and NiMo−$NiCu_{0.2}$ (47 mV dec^{-1}). These results suggest that the NiMo−NiCu composite presents higher catalytic activity and excellent HER kinetics when compared with Ni−Mo films. In addition, Tafel slope values near 42 mV dec^{-1} indicate that the reaction mechanism of HER at NiMo−NiCu is processed by the Volmer-Heyrovsky mechanism.[54] This mechanism is described as

$$H_2O + M + e^- \leftrightarrows MH_{ad} + OH^- \quad \text{Volmer step} \tag{2}$$

$$MH_{ad} + H_2O + e^- \rightarrow M + H_2 + OH^- \quad \text{Heyrovsky step} \tag{3}$$

Electrochemical impedance spectroscopy (EIS) technique was utilized to confirm the HER mechanism on the most active catalyst (NiMo−$NiCu_{0.12}$). EIS measurements are performed on the applied potentials of −0.978, −1.028, and −1.078 V vs Hg/HgO, i.e., HER overpotentials of −50, −100, and −150 mV. These values of overpotentials are chosen because there is no evolution of hydrogen in profusion, and thus little interference in the EIS measurements. The contribution of three semicircles (three-time constants) can be observed from the Nyquist and Bode diagrams (Figure 5c and d, respectively). Considering these results, the equivalent circuit model shown in Figure 5e is chosen to describe this system. It is seen that the time constant in high-frequency τ_1 (CPE_1 − R_2) which is independent of applied potential (the diagram of Bode) is associated to the film roughness and not with the reaction mechanism of HER. On the other hand, the time constants at lower frequencies τ_2 (CPE_2 − R_3) and τ_3 (CPE_3 − R_4) are related to charge transfer kinetics and to hydrogen adsorption, respectively.[18,33,55,56] The parameters obtained by adjusting the data with the equivalent circuit employed (Figure 5e) are shown in the Table S2. To calculate the values of the equivalent capacitances (C_1, C_2, and C_3) from the CPE_1, CPE_2, and CPE_3 parameters, equation S1 (in Supporting Information) of ref S6 is used.

Drawing a parallel between the impedance data and the HER mechanism, it has been shown that the values obtained for C_2 and R_3 are related to the response of double layer capacitance and the charge transfer resistance, the Heyrovsky step (eq 3). The C_3 and R_4 are indicated as the response of hydrogen adsorption pseudocapacitance and hydrogen adsorption resistance, Volmer's step (eq 2).[55,56] The parameters obtained show that an increase in the overpotential applied from −50 to −150 mV decreases the values of both C_2 and R_3. The value of C_2 decreased from 0.218 to 0.148 F cm^{-2}, while R_3 decreased from 0.409 to 0.273 Ω cm^{-2}. The decrease of C_2 is explained by taking into account the larger formation of gas bubbles with the increase of the overpotential and the consequent blockage of a larger portion of the electrode surface.[51] On the other hand, the decrease of R_3 featuring improved charge transfer with increasing overpotential. In contrast, the same increase in the overpotential more than doubles the value of C_3 (from 1.29 to 3.44 F cm^{-2}) and drastically reduces the value of R_4 (from 28.27 to 0.22 Ω cm^{-2}). Both the increase in C_3 value and the large reduction in R_4 value demonstrated that the hydrogen adsorption process (Volmer's step) is facilitated and the hydrogen evolution is ruled by the charge-transfer process (Heyrovsky's step) with the increase of the overpotential.[56] Therefore, as predicted by the Tafel slopes the mechanism of the hydrogen evolution reaction on NiMo−NiCu electrodes is processed by Volmer-Heyrovsky with Heyrovsky as the rate-determining step.

To compare the charge-transfer kinetics, interfacial properties, and the HER activity for all NiMo−NiCu electrodes, EIS was performed at −0.1 V vs reversible hydrogen electrode (RHE) in 6.0 mol L^{-1} KOH for prepared catalysts. The Nyquist diagram (Figure 6a) shows two semicircles; the semicircle in high frequencies (best seen in the insertion of Figure 6a) is attributed to surface roughness. On the other hand, the semicircle in low frequencies is related to charge-transfer process. Therefore, a two-time constant in series model (2TS) is used to describe this system. The fit data are available in the Table S3 (in SI).[33,55,56] As displayed in Table S3, NiMo−$NiCu_{0.12}$ film exhibits a lower charge-transfer resistance (R_{tc}) value (0.44 Ω cm^2) than NiMo (6.76 Ω cm^2), NiMo−$NiCu_{0.06}$ (1.27 Ω cm^2), and NiMo−$NiCu_{0.20}$ (0.520 Ω cm^2), indicating that NiMo−$NiCu_{0.12}$ has a much easier charge transfer, which leads to a higher hydrogen evolution than the other electrodes. Regardless of the amount of copper on the NiMo−NiCu electrodes, they have a much lower charge-transfer resistance than NiMo. This is caused by the higher surface roughness of NiMo−NiCu films, which makes contact between the electrode and the solution more efficient and increases not only the charge transfer but also the mass transfer.[32]

An excellent stability is a crucial feature for an electrocatalyst. Therefore, the continuous water electrolysis performance of NiMo and NiMo−$NiCu_{0.12}$ electrodes is investigated by chronopotentiometry at a current density of −100 mA cm^{-2} for 48 h in 6.0 mol L^{-1} KOH at 25 °C. As shown in Figure 6b, both electrodes have similar profiles in the electrolysis process, such that the NiMo−NiCu electrode has +80 mV of overpotential than NiMo electrode, indicating that the presence of Cu improves the catalytic activity of the Ni−Mo electrode. The first 8 h of electrolysis show that the potential maintains the current density in both electrodes and varies by only 20 mV at more negative potentials. The potential remains almost constant up to 48 h of electrolysis. This small variation of potential shows that both electrodes are very stable and do not suffer great wear of material by the process of hydrogen evolution.

The double layer capacitance (C_{dl}) of NiMo and NiMo−NiCu catalysts were measured by cyclic voltammetry (CV) in the non-Faradaic potential region (−0.6 to −0.7 V vs Hg/HgO) at different scan rates (10 to 150 mV s^{-1}),[30,31] the CV profiles can be seen in the Figure S4 (in SI). The plot of current density vs scan rate is shown at Figure S4 e (in SI). From the linear slope of Figure S4e, i.e., the C_{dl} values, the electrochemical active surface area (ECSA) was estimated. As seen in Figure 6c, ECSAs for NiMo−NiCu electrodes are much larger than NiMo electrodes. This is explained by taking into account the huge increase in surface roughness (over 30 times) with the insertion of copper into the NiMo film as shown by the AFM measurement (Figure 3). The larger effective area of NiMo−NiCu films consequently leads to greater electroactive area.[57] The NiMo−$NiCu_{0.12}$ film has the highest ECSA value (102.5 cm^2), followed by NiMo−$NiCu_{0.06}$ (91.75 cm^2), NiMo−$NiCu_{0.20}$ (91.5 cm^2), and NiMo (9.95 cm^2), this is consistent with the HER electrocatalytic activities of these electrodes. As observed by the SEM (Figure 2) and AFM (Figure 3) images, the coating morphology changed with

https://dx.doi.org/10.1021/acsami.0c00262
ACS Appl. Mater. Interfaces 2020, 12, 17492−17501

the copper concentration of the bath. For NiMo−$NiCu_{0.12}$, large pyramidal grains are observed (Figure 3b), while cauliflower shapes for NiMo−$NiCu_{0.20}$ were formed (Figure 2d). The cauliflower shapes probably present a minor contribution for the ECSA than pyramidal structures. Thus, the optimal condition studied for copper concentration in the bath was 0.12 mol L^{-1}.

For evaluating how the area of the materials influences the electrocatalytic activity of the films, Figure S5 shows the HER polarization curves normalized by ECSA instead of the geometric area, following the methodology of ref 32. It can be noted that all coatings showed a similar potential onset for HER indicating that the insertion of copper did not impact the intrinsic activity of NiMo. However, in higher current density, NiMo coating presents better activity per active site compared to NiMo−NiCu coatings. This fact indicates that the insertion of copper did not increase the number of active sites in proportion to the increase in surface area. In summary, the addition of copper has a strong influence on increasing the surface area, but not on the intrinsic activity of NiMo.

The effect of temperature on the catalytic activity of the coatings is evaluated by stationary cathodic polarization in KOH 6.0 mol L^{-1} at different temperatures for NiMo and for the catalyst with the best performance of HER (NiMo−$NiCu_{0.12}$) (Figure S6a,b in Supporting Information). Potentials of the reference electrode were corrected regarding the shift caused by the applied temperature. The variation of −1.206 mV K^{-1} was considered for the correction of electrode potentials.[58] Considering the calibration value of Hg/HgO vs RHE is −0.928 V at 25 °C (shown in Figure S2 in Supporting Information), Table S4 (in SI) presents the equations used to convert the measured potential to E vs RHE for each studied temperature. For both electrodes, the increase in electrolyte temperature leads to a pronounced effect of activity for the HER. The effect of temperature was more pronounced for NiMo coating, since a temperature variation of 40 K promotes 139 mV of overpotential decreasing to reach −100 mA cm^{-2}. In contrast, the overpotential decrease for the NiMo−$NiCu_{0.12}$ was 65 mV for the same current density. For both coatings, the Tafel curves are constructed and the exchange current densities (j_0) are estimated (Figure S6c,d, in Supporting Information). This parameter is important because it is directly proportional to the kinetic constants for each temperature. The curve obtained by log i_0 vs T^{-1} shows a linear relationship, allowing the apparent activation energy (ΔE_{at}) for the HER to be obtained by using the Arrhenius equation.[29] All exchange currents (i_0) obtained by Tafel curves were normalized by ECSA, aiming to eliminate the area effect, and the plot of log $j_{0\ ECSA}$ by T^{-1} is shown in Figure 6d. ΔE_{at} value calculated for the NiMo−NiCu coating is 21 kJ mol^{-1}, while for NiMo it is 22 kJ mol^{-1}, which indicates that the copper addition did not change the ΔE_{at} for HER. Xia et al.[20] found ΔE_{at} values of 21 kJ mol^{-1} and 26 kJ mol^{-1} for Ni−Mo−Cu and Ni−Mo alloys, respectively, very similar to the present results. In the literature, the synergism between Ni and Mo is well-known;[59] recently, there has been evidence of synergism between Ni and NiO_x. Sun et al.[32] demonstrated by first-principles DFT computational calculations that the Gibbs free energy of H adsorption (ΔG_{H^*}) (important parameter for evaluating intrinsic activity to HER) on the surfaces of $(NiO)_3$/Ni (ΔG_{H^*} = 0.08 eV) are closer to the optimal value for the maximum HER reaction rate (ΔG_{H^*} = 0.0 eV) compared to the Ni (111) surface (ΔG_{H^*} = −0.27 eV). This effect is explained by considering the electronegativity of the elements. Oxygen atoms being more electronegative attract the electrons from the d orbitals of Ni atoms leading to a decrease in the energy of H adsorption energy by these atoms.[32] Other studies have demonstrated the indispensable presence of the oxidized sites for superior HER electrocatalytic activity of certain materials in alkaline medium. In these cases, the oxides/hydroxides have bifunctional action, facilitating the dissociation of H_2O molecules and the production of H intermediates which subsequently migrate to active metal sites (e.g., $Ni(OH)_2$/Pt) that recombine into H_2 molecules.[60−62] Considering the above, an explanation is proposed for the high catalytic activity of the NiMo−NiCu composite. The large electro-active area due to copper, the synergism between Ni−Mo, and the presence of NiOOH and MoO_x on the NiMo−NiCu surface (as seen by XPS, Figure 4) that promote the free energy of H to an almost ideal value (that is, ΔG_{H^*} = 0.0 eV) and facilitate the adsorption and dissociation of H_2O molecules in the H intermediates are responsible for the high rate of HER reaction in these films.

4. CONCLUSION

NiMo and NiMo−NiCu composites were well produced by only a simple step of electrodeposition. In relation to morphology, the copper addition promoted an increase of 30 times on roughness of the surface, compared to NiMo. Copper distribution in the bulk and surface was confirmed by EDS, XRF, and XPS measurements. For XRD analyses, NiMo film presented a monocrystalline phase of $MoNi_4$, while all NiMo−NiCu coatings presented two different phases, attributed to $MoNi_4$ and NiCu, proving the interaction of only Ni−Cu and not the formation of Mo−Cu alloy.

All NiMo−NiCu materials showed higher electroactivity and stability of HER, compared to NiMo. The analyses on the area and temperature effects demonstrated that the copper addition did not change the active energy for HER, indicating that the improvement of catalytic activity for NiMo−NiCu materials is due to increasing electroactive area. The combination of the large electro-active area due to copper addition, the synergism between Ni−Mo, and the presence of Ni and Mo oxides on the surface results in catalyst with excellent features for HER application.

■ ASSOCIATED CONTENT

Supporting Information

The Supporting Information is available free of charge at https://pubs.acs.org/doi/10.1021/acsami.0c00262.

Rietveld refinement for samples, Calibration of the Hg/HgO reference electrode versus a hydrogen-saturated reference electrode, Electrocatalytic activities for different nickel-based cathodes for hydrogen evolution reaction, Point-to-point cathodic linear curves, Parameters obtained from the adjustment of the EIS data, Cyclic voltammetry, Point-to-point cathodic linear curves, Linear polarization curves, Equations used to convert the measured potential to E vs RHE at different temperatures (PDF)

■ AUTHOR INFORMATION

Corresponding Author

Lucia H. Mascaro − *Department of Chemistry, Federal University of São Carlos, 13565-905 São Carlos, São Paulo,*

https://dx.doi.org/10.1021/acsami.0c00262
ACS Appl. Mater. Interfaces 2020, 12, 17492−17501

Brazil; orcid.org/0000-0001-6908-1097;
Email: lmascaro@usfcar.br

Authors

Hugo L. S. Santos − *Department of Chemistry, Federal University of São Carlos, 13565-905 São Carlos, São Paulo, Brazil*

Patricia G. Corradini − *Department of Chemistry, Federal University of São Carlos, 13565-905 São Carlos, São Paulo, Brazil*

Marina Medina − *Department of Chemistry, Federal University of São Carlos, 13565-905 São Carlos, São Paulo, Brazil*

Jeferson A. Dias − *Department of Material Engineering, Federal University of São Carlos, 13565-905 São Carlos, São Paulo, Brazil*

Complete contact information is available at:
https://pubs.acs.org/10.1021/acsami.0c00262

Author Contributions

The manuscript was written through contributions of all authors. All authors have given approval to the final version of the manuscript.

Notes

The authors declare no competing financial interest.

■ ACKNOWLEDGMENTS

The authors thank the São Paulo Research Foundation (FAPESP) for financial assistance to the project and for the fellowships granted (grant 2018/16401-8, grant 2017/12794-2, grant 2017/11986-5, FAPESP/CDMF (2013/07296-2), Shell and the strategic importance of the support given by ANP (Brazil's National Oil, Natural Gas and Biofuels Agency) through the R&D levy regulation. The authors also wish to thank the Coordenação de Aperfeiçoamento de Pessoal de Nível Superior (CAPES) - Finance Code 001 and, by Conselho Nacional de Pesquisa e Desenvolvimento (CNPq 132040/2016-6; 141092/2018-1), for fellowships granted.

■ REFERENCES

(1) Ledendecker, M.; Mondschein, J. S.; Kasian, O.; Geiger, S.; Göhl, D.; Schalenbach, M.; Zeradjanin, A.; Cherevko, S.; Schaak, R. E.; Mayrhofer, K. Stability and Activity of Non-Noble-Metal-Based Catalysts toward the Hydrogen Evolution Reaction. *Angew. Chem., Int. Ed.* **2017**, *56* (33), 9767−9771.

(2) Zhang, L.; Xiong, K.; Nie, Y.; Wang, X.; Liao, J.; Wei, Z. Sputtering Nickel-Molybdenum Nanorods as an Excellent Hydrogen Evolution Reaction Catalyst. *J. Power Sources* **2015**, *297*, 413−418.

(3) Schalenbach, M.; Stolten, D. High-Pressure Water Electrolysis: Electrochemical Mitigation of Product Gas Crossover. *Electrochim. Acta* **2015**, *156*, 321−327.

(4) Yang, Q.; Dong, L.; Su, R.; Hu, B.; Wang, Z.; Jin, Y.; Wang, Y.; Besenbacher, F.; Dong, M. Nanostructured Heterogeneous Photo-Catalysts for Hydrogen Production and Water Splitting: A Comprehensive Insight. *Applied Materials Today* **2019**, *17*, 159−182.

(5) Kublanovsky, V. S.; Yapontseva, Y. S. Electrocatalytic Properties of Co-Mo Alloys Electrodeposited from a Citrate-Pyrophosphate Electrolyte. *Electrocatalysis* **2014**, *5* (4), 372−378.

(6) Marceta Kaninski, M. P.; Miulovic, S. M.; Tasic, G. S.; Maksic, A. D.; Nikolic, V. M. A Study on the Co-W Activated Ni Electrodes for the Hydrogen Production from Alkaline Water Electrolysis - Energy Saving. *Int. J. Hydrogen Energy* **2011**, *36* (9), 5227−5235.

(7) Murthy, A. P.; Madhavan, J.; Murugan, K. Recent Advances in Hydrogen Evolution Reaction Catalysts on Carbon/Carbon-Based Supports in Acid Media. *J. Power Sources* **2018**, *398*, 9−26.

(8) Wen, X.; Guan, J. Recent Progress on Mof-Derived Electrocatalysts for Hydrogen Evolution Reaction. *Applied Materials Today* **2019**, *16*, 146−168.

(9) Bocca, C.; Barbucci, A.; Cerisola, G. The Influence of Surface Finishing on the Electrocatalytic Properties of Nickel for the Oxygen Evolution Reaction (Oer) in Alkaline Solution. *Int. J. Hydrogen Energy* **1998**, *23* (4), 247−252.

(10) Mauer, A. E.; Kirk, D. W.; Thorpe, S. J. The Role of Iron in the Prevention of Nickel Electrode Deactivation in Alkaline Electrolysis. *Electrochim. Acta* **2007**, *52* (11), 3505−3509.

(11) Santos, D. M. F.; Sequeira, C. A. C.; Figueiredo, J. L. Hydrogen Production by Alkaline Water Electrolysis. *Quim. Nova* **2013**, *36* (8), 1176−1193.

(12) Schalenbach, M.; Zeradjanin, A. R.; Kasian, O.; Cherevko, S.; Mayrhofer, K. J. J. A Perspective on Low-Temperature Water Electrolysis - Challenges in Alkaline and Acidic Technology. *Int. J. Electrochem. Sci.* **2018**, *13* (2), 1173−1226.

(13) Jaksic, M. M. Electrocatalysis of Hydrogen Evolution in the Light of the Brewer-Engel Theory for Bonding in Metals and Intermetallic Phases. *Electrochim. Acta* **1984**, *29* (11), 1539−1550.

(14) Kita, H.; Kurisu, T. Electrocatalysis by D and Sp Metals. *Journal of the Research Institute for Catalysis* **1973**, *21* (3), 200−246.

(15) CONWAY, B. E.; BOCKRIS, J. O. Electrolytic Hydrogen Evolution Kinetics and Its Relation to the Electronic and Adsorptive Properties of the Metal. *J. Chem. Phys.* **1957**, *26* (3), 532−541.

(16) Casciano, P. N. S.; Benevides, R. L.; Santana, R. A. C.; Correia, A. N.; de Lima-Neto, P. Factorial Design in the Electrodeposition of Co-Mo Coatings and Their Evaluations for Hydrogen Evolution Reaction. *J. Alloys Compd.* **2017**, *723*, 164−171.

(17) Sanches, L. S.; Domingues, S. H.; Carubelli, A.; Mascaro, L. H. Electrodeposition of Ni-Mo and Fe-Mo Alloys from Sulfate-Citrate Acid Solutions. *J. Braz. Chem. Soc.* **2003**, *14* (4), 556−563.

(18) Navarro-Flores, E.; Chong, Z. W.; Omanovic, S. Characterization of Ni, Nimo, Niw and Nife Electroactive Coatings as Electrocatalysts for Hydrogen Evolution in an Acidic Medium. *J. Mol. Catal. A: Chem.* **2005**, *226* (2), 179−197.

(19) Wang, K. C.; Xia, M.; Xiao, T.; Lei, T.; Yan, W. S. Metallurgically Prepared Nicu Alloys as Cathode Materials for Hydrogen Evolution Reaction. *Mater. Chem. Phys.* **2017**, *186*, 61−66.

(20) Xia, M.; Lei, T.; Lv, N. L.; Li, N. F. Synthesis and Electrocatalytic Hydrogen Evolution Performance of Ni-Mo-Cu Alloy Coating Electrode. *Int. J. Hydrogen Energy* **2014**, *39* (10), 4794−4802.

(21) Wang, Z.; Ge, X.; Li, Z.; Wu, J.; Liang, Z.; Wang, S. Mo-Doped Nicu as an Efficient and Stable Electrocatalyst for the Hydrogen Evolution Reaction. *New J. Chem.* **2019**, *43* (24), 9652−9657.

(22) Li, Y.; Zhang, X.; Hu, A.; Li, M. Morphological Variation of Electrodeposited Nanostructured Ni-Co Alloy Electrodes and Their Property for Hydrogen Evolution Reaction. *Int. J. Hydrogen Energy* **2018**, *43* (49), 22012−22020.

(23) Goranova, D.; Lefterova, E.; Rashkov, R. Electrocatalytic Activity of Ni-Mo-Cu and Ni-Co-Cu Alloys for Hydrogen Evolution Reaction in Alkaline Medium. *Int. J. Hydrogen Energy* **2017**, *42* (48), 28777−28785.

(24) Medina, M.; Corradini, P. G.; Mascaro, L. H. Facile One-Step Electrodeposition Fabrication of Amorphous Mos2 Catalysts in Titanium for Hydrogen Evolution Reaction. *J. Braz. Chem. Soc.* **2019**, 1−9.

(25) Zheng, Z.; Li, N.; Wang, C.-Q.; Li, D.-Y.; Meng, F.-Y.; Zhu, Y.-M.; Li, Q.; Wu, G. Electrochemical Synthesis of Ni−S/Ceo2 Composite Electrodes for Hydrogen Evolution Reaction. *J. Power Sources* **2013**, *230*, 10−14.

(26) Shetty, S.; Mohamed Jaffer Sadiq, M.; Bhat, D. K.; Hegde, A. C. Electrodeposition and Characterization of Ni-Mo Alloy as an Electrocatalyst for Alkaline Water Electrolysis. *J. Electroanal. Chem.* **2017**, *796*, 57−65.

(27) Beltowska-Lehman, E. Electrodeposition of Protective Ni-Cu-Mo Coatings from Complex Citrate Solutions. *Surf. Coat. Technol.* **2002**, *151*, 440−443.

(28) Necas, D.; Klapetek, P. Gwyddion: An Open-Source Software for Spm Data Analysis. *Cent Eur. J. Phys.* **2012**, *10* (1), 181−188.
(29) Bockris, J. O. M.; Potter, E. C. The Mechanism of the Cathodic Hydrogen Evolution Reaction. *J. Electrochem. Soc.* **1952**, *99* (4), 169−186.
(30) McCrory, C. C. L.; Jung, S.; Peters, J. C.; Jaramillo, T. F. Benchmarking Heterogeneous Electrocatalysts for the Oxygen Evolution Reaction. *J. Am. Chem. Soc.* **2013**, *135* (45), 16977−16987.
(31) Li, Y.; Zhao, C. Enhancing Water Oxidation Catalysis on a Synergistic Phosphorylated Nife Hydroxide by Adjusting Catalyst Wettability. *ACS Catal.* **2017**, *7* (4), 2535−2541.
(32) Sun, Q. Q.; Dong, Y. J.; Wang, Z. L.; Yin, S. W.; Zhao, C. Synergistic Nanotubular Copper-Doped Nickel Catalysts for Hydrogen Evolution Reactions. *Small* **2018**, *14* (14), 1704137.
(33) Kubisztal, J.; Budniok, A.; Lasia, A. Study of the Hydrogen Evolution Reaction on Nickel-Based Composite Coatings Containing Molybdenum Powder. *Int. J. Hydrogen Energy* **2007**, *32* (9), 1211−1218.
(34) Kumar, A.; Jayasankar, K.; Debata, M.; Mandal, A. Mechanical Alloying and Properties of Immiscible Cu-20 Wt.% Mo Alloy. *J. Alloys Compd.* **2015**, *647*, 1040−1047.
(35) Yin, Z.; Chen, F. A Facile Electrochemical Fabrication of Hierarchically Structured Nickel−Copper Composite Electrodes on Nickel Foam for Hydrogen Evolution Reaction. *J. Power Sources* **2014**, *265*, 273−281.
(36) Gutic, S. J.; Jovanovic, A. Z.; Dobrota, A. S.; Metarapi, D.; Rafailovic, L. D.; Pasti, I. A.; Mentus, S. V. Simple Routes for the Improvement of Hydrogen Evolution Activity of Ni-Mo Catalysts: From Sol-Gel Derived Powder Catalysts to Graphene Supported Co-Electrodeposits. *Int. J. Hydrogen Energy* **2018**, *43* (35), 16846−16858.
(37) Landolt, D. Fundamental Aspects of Alloy Plating. *Plat Surf. Finish* **2001**, *88* (9), 70−79.
(38) Han, X.; Xu, D.; An, L.; Hou, C.; Li, Y.; Zhang, Q.; Wang, H. Ni-Mo Nanoparticles as Co-Catalyst for Drastically Enhanced Photocatalytic Hydrogen Production Activity over G-C3n4. *Appl. Catal., B* **2019**, *243*, 136−144.
(39) Biesinger, M. C.; Payne, B. P.; Grosvenor, A. P.; Lau, L. W. M.; Gerson, A. R.; Smart, R. S. C. Resolving Surface Chemical States in Xps Analysis of First Row Transition Metals, Oxides and Hydroxides: Cr, Mn, Fe, Co and Ni. *Appl. Surf. Sci.* **2011**, *257* (7), 2717−2730.
(40) Wang, Y.; Wang, J.; Xie, T.; Zhu, Q.; Zeng, D.; Li, R.; Zhang, X.; Liu, S. Ru Doping in Ni(Oh)2 to Accelerate Water Reduction Kinetics for Efficient Hydrogen Evolution Reaction. *Appl. Surf. Sci.* **2019**, *485*, 506−512.
(41) Sharma, L.; Khushwaha, H. S.; Mathur, A.; Halder, A. Role of Molybdenum in Ni-Moo2 Catalysts Supported on Reduced Graphene Oxide for Temperature Dependent Hydrogen Evolution Reaction. *J. Solid State Chem.* **2018**, *265*, 208−217.
(42) Sanches, L. S.; Domingues, S. H.; Carubelli, A.; Mascaro, L. H. Electrodeposition of Ni-Mo and Fe-Mo Alloys from Sulfate-Citrate Acid Solutions. *J. Braz. Chem. Soc.* **2003**, *14*, 556−563.
(43) Sanches, L. S.; Domingues, S. H.; Marino, C. E. B.; Mascaro, L. H. Characterisation of Electrochemically Deposited Ni−Mo Alloy Coatings. *Electrochem. Commun.* **2004**, *6* (6), 543−548.
(44) Winiarski, J.; Tylus, W.; Winiarska, K.; Szczygieł, B. The Influence of Molybdenum on the Corrosion Resistance of Ternary Zn−Co−Mo Alloy Coatings Deposited from Citrate−Sulphate Bath. *Corros. Sci.* **2015**, *91*, 330−340.
(45) Sen, B.; Kuyuldar, E.; Savk, A.; Calimli, H.; Duman, S.; Sen, F. Monodisperse Ruthenium-Copper Alloy Nanoparticles Decorated on Reduced Graphene Oxide for Dehydrogenation of Dmab. *Int. J. Hydrogen Energy* **2019**, *44* (21), 10744−10751.
(46) Zhu, J.; Chen, C.; Li, Y.; Zhou, L.; Lan, Y. Rapid Degradation of Aniline by Peroxydisulfate Activated with Copper-Nickel Binary Oxysulfide. *Sep. Purif. Technol.* **2019**, *209*, 1007−1015.
(47) Biesinger, M. C. Advanced Analysis of Copper X-Ray Photoelectron Spectra. *Surf. Interface Anal.* **2017**, *49* (13), 1325−1334.
(48) Li, W.; Shen, X.; Zeng, R.; Chen, J.; Xiao, W.; Ding, S.; Chen, C.; Zhang, R.; Zhang, N. Constructing Copper-Ceria Nanosheets with High Concentration of Interfacial Active Sites for Enhanced Performance in Co Oxidation. *Appl. Surf. Sci.* **2019**, *492*, 818.
(49) Che, Q.; Li, Q.; Tan, Y.; Chen, X.; Xu, X.; Chen, Y. One-Step Controllable Synthesis of Amorphous (Ni-Fe)Sx/Nife(Oh)Y Hollow Microtube/Sphere Films as Superior Bifunctional Electrocatalysts for Quasi-Industrial Water Splitting at Large-Current-Density. *Appl. Catal., B* **2019**, *246*, 337−348.
(50) Anjum, M. A. R.; Lee, M. H.; Lee, J. S. Boron- and Nitrogen-Codoped Molybdenum Carbide Nanoparticles Imbedded in a Bcn Network as a Bifunctional Electrocatalyst for Hydrogen and Oxygen Evolution Reactions. *ACS Catal.* **2018**, *8* (9), 8296−8305.
(51) Wang, H.; Lee, H.-W.; Deng, Y.; Lu, Z.; Hsu, P.-C.; Liu, Y.; Lin, D.; Cui, Y. Bifunctional Non-Noble Metal Oxide Nanoparticle Electrocatalysts through Lithium-Induced Conversion for Overall Water Splitting. *Nat. Commun.* **2015**, *6*, 7261.
(52) Wang, L.; Cao, J.; Lei, C.; Dai, Q.; Yang, B.; Li, Z.; Zhang, X.; Yuan, C.; Lei, L.; Hou, Y. Strongly Coupled 3d N-Doped Moo2/Ni3s2 Hybrid for High Current Density Hydrogen Evolution Electrocatalysis and Biomass Upgrading. *ACS Appl. Mater. Interfaces* **2019**, *11* (31), 27743−27750.
(53) Zhang, K. Y.; Xiao, W.; Li, J. Y.; Liu, J. G.; Yan, C. W. Two-Step Preparation of Porous Nickel-Sulfur Electrode for Hydrogen Evolution in Alkaline Water Electrolysis. *Electrochim. Acta* **2017**, *228*, 422−427.
(54) Conway, B. E.; Tilak, B. V. Interfacial Processes Involving Electrocatalytic Evolution and Oxidation of H2, and the Role of Chemisorbed H. *Electrochim. Acta* **2002**, *47* (22), 3571−3594.
(55) Birry, L.; Lasia, A. Studies of the Hydrogen Evolution Reaction on Raney Nickel-Molybdenum Electrodes. *J. Appl. Electrochem.* **2004**, *34* (7), 735−749.
(56) Herraiz-Cardona, I.; Ortega, E.; Perez-Herranz, V. Impedance Study of Hydrogen Evolution on Ni/Zn and Ni-Co/Zn Stainless Steel Based Electrodeposits. *Electrochim. Acta* **2011**, *56* (3), 1308−1315.
(57) Wang, L.; Li, Y.; Xia, M.; Li, Z.; Chen, Z.; Ma, Z.; Qin, X.; Shao, G. Ni Nanoparticles Supported on Graphene Layers: An Excellent 3d Electrode for Hydrogen Evolution Reaction in Alkaline Solution. *J. Power Sources* **2017**, *347*, 220−228.
(58) Bratsch, S. G. Standard Electrode Potentials and Temperature Coefficients in Water at 298.15 K. *J. Phys. Chem. Ref. Data* **1989**, *18* (1), 1−21.
(59) McKay, I. S.; Schwalbe, J. A.; Goodman, E. D.; Willis, J. J.; Majumdar, A.; Cargnello, M. Elucidating the Synergistic Mechanism of Nickel−Molybdenum Electrocatalysts for the Hydrogen Evolution Reaction. *MRS Commun.* **2016**, *6* (3), 241−246.
(60) Danilovic, N.; Subbaraman, R.; Strmcnik, D.; Chang, K.-C.; Paulikas, A. P.; Stamenkovic, V. R.; Markovic, N. M. Enhancing the Alkaline Hydrogen Evolution Reaction Activity through the Bifunctionality of Ni(Oh)2/Metal Catalysts. *Angew. Chem., Int. Ed.* **2012**, *51* (50), 12495−12498.
(61) Subbaraman, R.; Tripkovic, D.; Chang, K.-C.; Strmcnik, D.; Paulikas, A. P.; Hirunsit, P.; Chan, M.; Greeley, J.; Stamenkovic, V.; Markovic, N. M. Trends in Activity for the Water Electrolyser Reactions on 3d M(Ni,Co,Fe,Mn) Hydr(Oxy)Oxide Catalysts. *Nat. Mater.* **2012**, *11* (6), 550−557.
(62) Subbaraman, R.; Tripkovic, D.; Strmcnik, D.; Chang, K.-C.; Uchimura, M.; Paulikas, A. P.; Stamenkovic, V.; Markovic, N. M. Enhancing Hydrogen Evolution Activity in Water Splitting by Tailoring Li^+-Ni$(Oh)_2$-Pt Interfaces. *Science* **2011**, *334* (6060), 1256−1260.

https://dx.doi.org/10.1021/acsami.0c00262
ACS Appl. Mater. Interfaces 2020, 12, 17492−17501